Enhancement of $LiVPO_4F$ cathode materials via manganese doping: Boosting energy density and rate capability for high-voltage lithium-ion batteries

Ismail Assengar [a,b], Sylvio Indris [b,c], Arseniy Bokov [c,d], Liuda Mereacre [c], Mohammed Mansori [a], Ismael Saadoune [b,*]

[a] Innovative Materials, Energy and Development Laboratory (IMED-Lab), Chemistry Department, Cadi Ayyad University, Marrakech, Morocco
[b] Applied Chemistry and Engineering Research Centre of Excellence (ACER CoE), Mohammed VI Polytechnic University, Ben Guerir, Morocco
[c] Institute for Applied Materials (IAM) Karlsruhe Institute of Technology (KIT), Hermann-von-Helmholtz-Platz 1, Eggenstein-Leopoldshafen 76344, Germany
[d] Karlsruhe Institute of Technology (KIT), Helmholtz Institute Ulm - Electrochemical Energy Storage (HIU-EES), Helmholtz Strasse 11, Ulm 89081, Germany

Keywords:
Li-ion batteries
Fluoro-phosphates
High voltage cathodes
High energy density, One-step sol-gel synthesis

A B S T R A C T

High-voltage fluorophosphate cathode materials have emerged as promising candidates for next-generation lithium-ion batteries, offering enhanced safety, energy density, and stability compared to conventional oxide-based materials. In this study we investigate the effects of manganese doping on the structural and electrochemical properties of $LiVPO_4F$ cathode material synthesized via an optimized and simple sol-gel method. A series of $LiV_{1-2y/3}Mn_yPO_4F/C$ (y 0, 0.03, 0.09, 0.15) compositions was successfully prepared and characterized to highlight the impact of Mn substitution on structural stability and electrochemical performance. X-ray diffraction analysis confirmed the preservation of the initial crystal structure of the undoped material for manganese content up to y 0.09, while higher concentration (y 0.15) leads to the appearance of secondary phases. The successful incorporation of Mn was confirmed by systematic shifts in diffraction peaks and changes in the unit cell parameters. Electrochemical characterization revealed that the optimized composition (y 0.09) delivered a remarkable discharge capacity of 150 mAh/g at C/5, approaching the theoretical capacity of 153 mAh/g, with 98 % capacity retention after 100 cycles. Notably, all compositions demonstrated excellent thermal stability at 50 °C. Once again, the composition corresponding to y 0.09 shows the best performance as it maintains a discharge capacity of 149 mAh/g with minimal capacity fade (≈0.7 %) after 50 cycles. Rate capability tests showed enhanced performance for Mn-doped samples, particularly at higher C-rates, attributed to improved charge transfer kinetics and structural stability. The enhanced performance is attributed to the synergistic effects of successful Mn incorporation and the uniform carbon coating derived from the in-situ carbonization of citric acid. These results demonstrate the effectiveness of our synthetic approach in developing high-performance cathode materials for advanced lithium-ion batteries.

1. Introduction

The surge in portable devices, electric vehicles, and grid energy storage has driven an evolving demand for reliable and efficient energy storage solutions. Lithium-ion batteries (LIBs) have emerged as dominant technology in this field, offering high energy density, durability, and comparatively low capacity fade [1]. However, the performance and efficiency of LIBs are largely tied to the properties of their cathode materials, which play a significant role in defining the battery's energy density, cycle life, and stability. Thus, continuous research and development in cathode materials remain essential for further improving LIBs capabilities and satisfying the growing energy storage demands.

Currently, commercial LIBs primarily utilize transition metal oxide cathodes such as $LiCoO_2$ and $Li(Ni_{1-x-y}Mn_xCo_y)O_2$ (NMC) [2,3]. While these oxides have achieved commercial success, they face notable limitations, particularly in terms of rapid voltage decay with cycling, rate capability, low safety and high cost (especially due to cobalt content) [4]. To address these issues, spinel oxides, LiM_2O_4, and layered oxides, $LiMO_2$ (where M= Co, Ni, Mn, Al), have been developed, offering higher

* Corresponding author.
E-mail address: Ismael.SAADOUNE@um6p.ma (I. Saadoune).

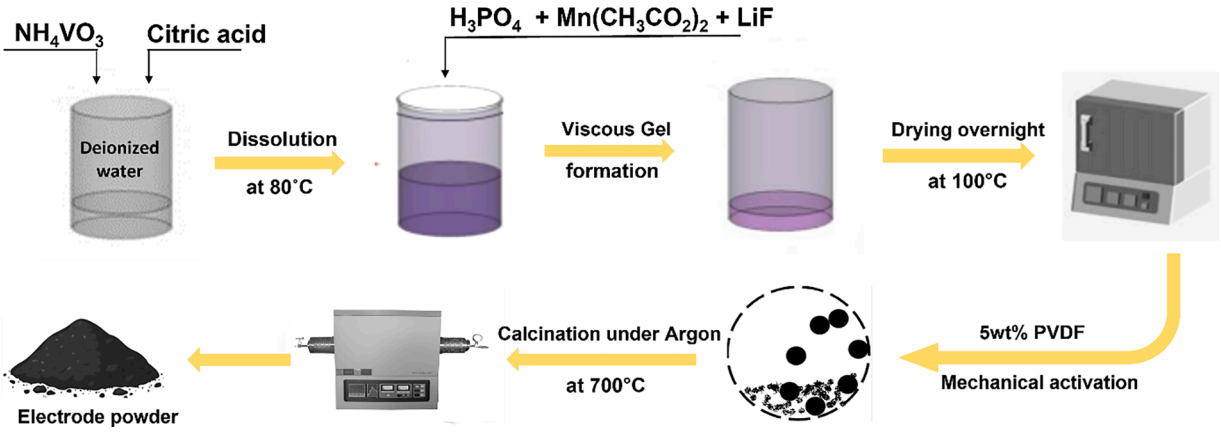

Fig. 1. Schematic illustration of the sol-gel synthesis process for $LiV_{1-2y/3}Mn_yPO_4F/C$ cathode materials.

operating voltage (>4.3 V) and improved theoretical capacities [5,6]. However, these high-voltage oxides are limited by low thermal stability, as fast charging can lead to the formation of metastable phases prone to decomposition and oxygen release, raising safety concerns. In addition, their sensitivity to moisture makes them hard to process and can significantly shorten their lifetime. Furthermore, Mn-dissolution from the cathode into the electrolyte during cycling leads to poor electrochemical performance, resulting in capacity fading [7,8].

To address these challenges, extensive studies have been conducted by researchers worldwide investigating polyanion-based cathode materials as promising alternatives. These compounds, which include phosphates, sulfates, and silicates, offer enhanced structural stability due to the strong covalent bonding within the polyanion groups (e.g., PO_4^{3-}, SiO_4^{4-}, SO_4^{2-}), and potentially higher operating voltages compared to their oxide counterparts. These improvements can enhance the safety and lifespan of the batteries [9]. Among these, $LiFePO_4$ (LFP), a widely used cathode material in lithium-ion batteries, is renowned for its excellent safety and stability due to its robust olivine structure, which minimizes thermal runaway risks [10,11]. However, LFP has a relatively low operating voltage of approximately 3.4 V versus Li/Li^+ [12]. Consequently, while LFP is favored for applications where safety is paramount, such as in electric vehicles and stationary energy storage systems, its lower working voltage remains a significant drawback when higher energy densities are required.

In the quest for high voltage yet stable cathode materials, fluorophosphates-based materials have emerged as promising electrode materials due to the covalent character of phosphate group with the strong P-O bonds, that creates a robust framework resistant to decomposition, even at high voltage. Furthermore, the high electronegativity of the fluorine atom with the strong inductive effect modifies the electronic structure of the transition metal, effectively lowering the energy of its d-orbitals. This lowers the d-orbital energy, enhancing the metal redox potential and enabling higher operating voltages compared to non-fluorinated phosphates [13,14]. Among various candidate fluorophosphate-based materials for application as cathodes in Li-ion secondary batteries, lithium vanadium fluorophosphate $LiVPO_4F$ has gained the most attention owing to its high theoretical capacity of 156 mAh/g with a potential plateau of 4.28 V vs. Li/Li^+ resulting in high energy density (655 Wh kg^{-1}, based on the cathode mass). Additionally, vanadium's ability to undergo multivalent electrochemical conversions further contributes to the material's suitability for high-performance lithium-ion batteries [15].

Two common synthetic approaches have been reported in the literature to prepare this type of materials: a two-step solid-state reaction process involving separate preparation of VPO4 intermediate followed by LiF addition prior to high-temperature calcination [16,17], and a one-step sol-gel route where precursors are directly mixed in the process [18]. However, the synthesis of a pure fluorophosphate phase is challenging, as improper regulation of experimental conditions, such as temperature, calcination time, and precursor ratios can lead to the material's decomposition into more stable phases, mainly the NaSICon phase $Li_3V_2(PO_4)_3$ [19,20]. Furthermore, the introduction of dopants can complicate the synthesis and increase the risk of forming undesired secondary phases, or lead to the suppression of the intended phase by the dominant olivine structure [21].

In the pursuit of achieving the full electrochemical potential of $LiVPO_4F$ cathode material, numerous strategies, including metal doping [21–23], applying coatings of conductive materials like carbon and metal [24–27], as well as optimizing particle size and morphology through precise synthesis conditions [28,29], have been investigated. While some studies have reported improvements over the undoped material, these enhancements still fall short of the phase's theoretical potential, possibly due to synthesis challenges or vanadium-dopant incompatibilities.

Exploring manganese as a dopant has shown promising potential in enhancing the structural integrity and cycling efficiency of vanadium-based polyanionic cathode materials. It was demonstrated that Mn^{3+} doping in $Li_3V_2(PO_4)_3$ can help reducing the band gap energy, improving the electronic properties of the material [30]. Additionally, doping the same phase with Mn^{2+} enhances the cyclic stability and rate performance even at high rates, as electrochemical impedance spectroscopy (EIS) reveals that Mn^{2+} doping decreases the charge transfer resistance, facilitating faster lithium-ion insertion and extraction [31]. The beneficial effects of manganese doping have also been observed in Na-ion battery materials, where Mn^{3+} doping in $Na_{2.85}Mn_{0.4}V_{1.6}(PO_4)_2F_{2.4}O_{0.6}$ stabilizes the structure and improves capacity retention, especially at high cycling rates [32]. Furthermore, Mn^{2+} doping in $Na_3V_2(PO_4)_3$ significantly enhances its performance by mitigating the material's low intrinsic conductivity. This modification allows for greater Na^+ insertion, resulting in a higher reversible capacity [33]. The compatibility between manganese and vanadium in these polyanionic cathode materials is a key factor contributing to the success of Mn-doping strategies.

In this study, we explore the effects of manganese substitution on the structural and electrochemical properties of $LiVPO_4F$ synthesized using a one-step sol-gel method. Our research emphasizes optimizing synthesis conditions to obtain phase-pure Mn-doped $LiVPO_4F$ with a mixed-valence system while analyzing the influence of Mn doping on the material's crystal structure, morphology, and electrochemical behavior. Special attention is given to the relationship between dopant concentration and cycling stability across different C-rates, with the goal of determining the optimal composition for improved battery performance.

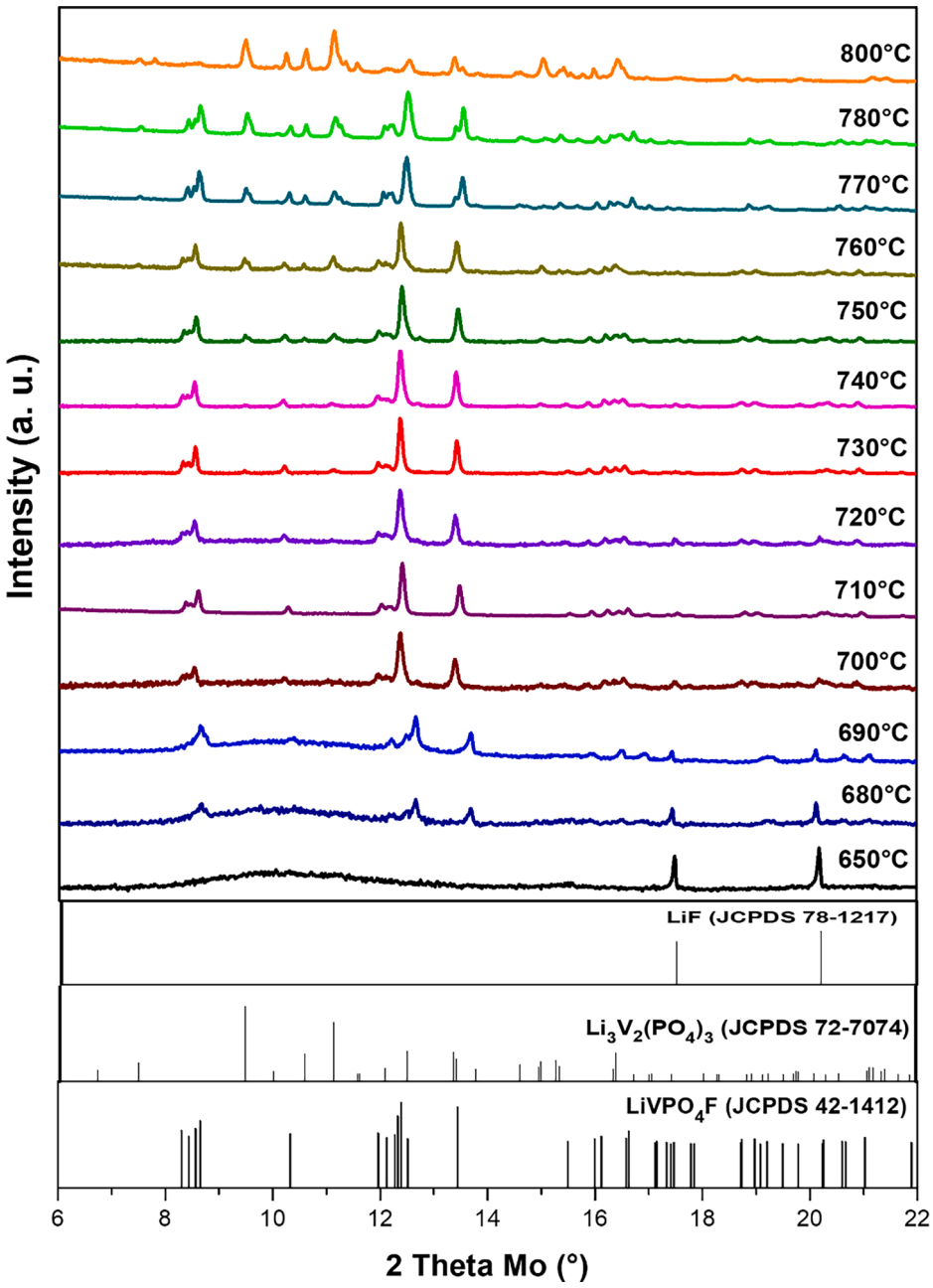

Fig. 2. (a). In-situ XRD patterns of $LiVPO_4F$ precursors mixture as a function of temperature.

2. Experimental section

2.1. Material synthesis

As described in Fig. 1, $LiV_{1-2y/3}Mn_yPO_4F/C$ ($y = 0, 0.03, 0.09, 0.15$) cathode materials series has been successfully synthesized through a water-based sol-gel method. 1:2 stoichiometric amounts of NH_4VO_3 (Sigma Aldrich, 99 %) and citric acid (VWR Chemicals, 99 %), serving simultaneously as chelating agent, reducing agent, and carbon source, were first dissolved in 40 mL of deionized water at 80 °C under stirring for 10 min to obtain a green solution indicating the reduction of V^{5+} to V^{3+}. Subsequently, $Mn(CH_3CO_2)_2$ (Sigma Aldrich, 99 %), H_3PO_4, and LiF (Sigma Aldrich, 99 %) were added to the solution and stirred for a 4 h. 2 % excess of LiF was added in order to compensate for lithium and fluorine loss during calcination. After the formation of the gel, it was dried at 100 °C overnight. The obtained blue xerogel was then ball-milled with 5wt % of polyvinylidene difluoride (PVDF) for 2 h at 500 rpm. The recovered powder was transferred to an alumina boat and heated under argon atmosphere at 700 °C for 1 hour followed by quenching to room temperature under the same atmosphere, to obtain the final product.

2.2. Material characterization

The crystal structure of the prepared samples was investigated via X-ray diffraction (XRD) using a STOE Stadi P diffractometer with a Cu Kα1 radiation source. The measurements were conducted at 40 kV and 40 mA in transmission mode. The crystallographic parameters were obtained by the Rietveld method using FULLPROF software.

To investigate the presence of carbon on the synthesized cathode materials, Raman Spectroscopy technique was employed using a Lab-RAM HR Evolution Raman spectrometer (HORIBA Scientific) with red light laser (wavelength $\lambda = 632.81$ nm).

The morphology, grain size and elemental distribution of the

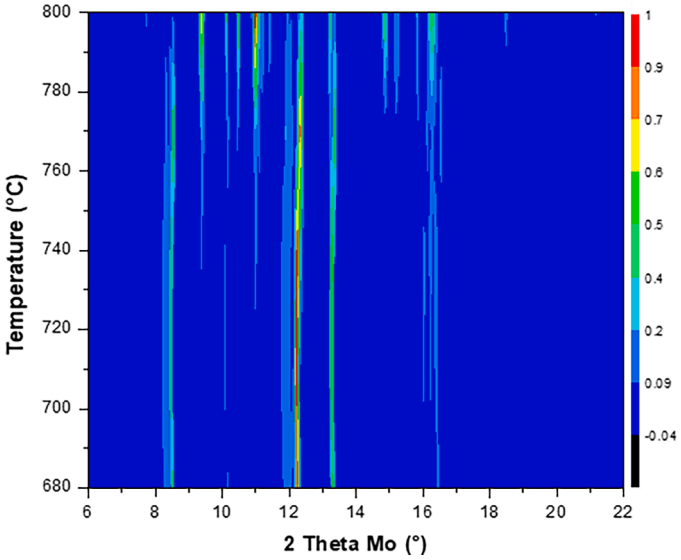

Fig. 2. (b). 2D Contour plot of in-situ XRD measurement of $LiVPO_4F$ precursors mixture as a function of temperature.

obtained particles in the synthesized samples were observed using scanning electron microscopy (SEM) (ZEISS, GEMINI 1530) and energy dispersive X-ray spectroscopy (EDS) with an accelerating voltage of 20 kV.

2.3. Electrochemical measurements

The positive electrodes were prepared by mixing the active material, poly(vinylidene difluoride) (Mw=250 K, Sigma Aldrich) and carbon black (Sigma Alrich) with a weight ratio of 75:10:15, respectively. The mixture was initially hand-ground in an agate mortar for 10 min, followed by the addition of NMP solvent and continuous magnetic stirring overnight. The resulting slurry was then coated onto aluminum foil and dried in a vacuum oven at 100 °C for 2 h to remove the solvent. Subsequently, a 12 mm disk was then punched out from the electrode and dried under vacuum at 70 °C overnight prior to battery assembling. The mass loading is approximately 2.5 mg/cm^2. In an argon-filled glove box, CR2032 coin-type cells were assembled using the positive electrode, 1 cm^2 metallic Lithium disk as the negative electrode, Celgard membrane as the separator and 1 M of $LiPF_6$ in EC-DMC (1:1) as the electrolyte.

The electrochemical performance of $LiV_{1-2y/3}MnyPO_4F/C$ cathode materials was assessed within a voltage range of 3 V to 4.6 V vs. Li^+/Li at various current rates (0.2C to 5C) using a BioLogic MPG2 battery cycler. Measurements were conducted at both room temperature (25 °C) and an elevated temperature of 50 °C.

3. Results and discussion

3.1. Crystal structure and morphology

Fig. 2 depicts the in-situ XRD patterns of various lithium-based compounds, including LiF, $Li_3V_2(PO_4)_3$, and $LiVPO_4F$, across a temperature range from 650 °C to 800 °C. At 650 °C, the XRD patterns show an amorphous mixture with some peaks corresponding to the LiF phase, indicating the initial state of the sample. As the temperature increases, the LiVPO4F phase forms and becomes dominant between 690 °C and 740 °C. The sharp, well-defined peaks observed in this temperature interval confirm the successful synthesis of the crystalline $LiVPO_4F$ structure. However, when the temperature exceeds 740 °C, the $LiVPO_4F$ phase begins to decompose. The emergence of peaks associated with the $Li_3V_2(PO_4)_3$ phase at higher temperatures indicates that the $LiVPO_4F$ compound becomes unstable and starts to decompose, likely due to fluorine loss at elevated temperatures [19]. These findings highlight the importance of the temperature window for the formation of the $LiVPO_4F$ phase. The optimal temperature range appears to be 700 °C, as this is the lowest temperature where the $LiVPO_4F$ phase is successfully synthesized and stabilized. Higher temperatures lead to the decomposition of $LiVPO_4F$ and the formation of the secondary $Li_3V_2(PO_4)_3$ phase.

Fig. 2a, Fig. 2b.

As displayed in Fig. 3. **(a)**, the main phase of all samples is in good agreement with the phase $LiVPO_4F$ with triclinic crystal system and space group P-1 as reported in literature. This means that the addition of a small amount of manganese does not significantly affect the crystal structure of $LiVPO_4F/C$ [34,35]. However, at a high Mn substitution ratio ($y = 0.15$), the formation of the $LiMnPO_4$ phase becomes unavoidable under the given synthesis conditions. Furthermore, in the sample V-Mn15, a very small amount of $Li_3V_2(PO_4)_3$ is detected corresponding to the diffraction peaks located at 20.7°, 24.4°, and 33.1°, likely due to the alteration of stoichiometry following the formation of $LiMnPO_4$ and to the sublimation of VF_3 during calcination[36]. The diffraction peaks of carbon are not observed in the XRD spectra of each sample, which shows that the rest of the carbon is amorphous.

The effect of Mn doping on $LiVPO_4F$ is obvious across different manganese contents ($y = 0$, 0.03, 0.09, and 0.15). As shown in Fig. 3. **(b),** the (1–10) reflection peak, a characteristic peak of the LiVPO4F

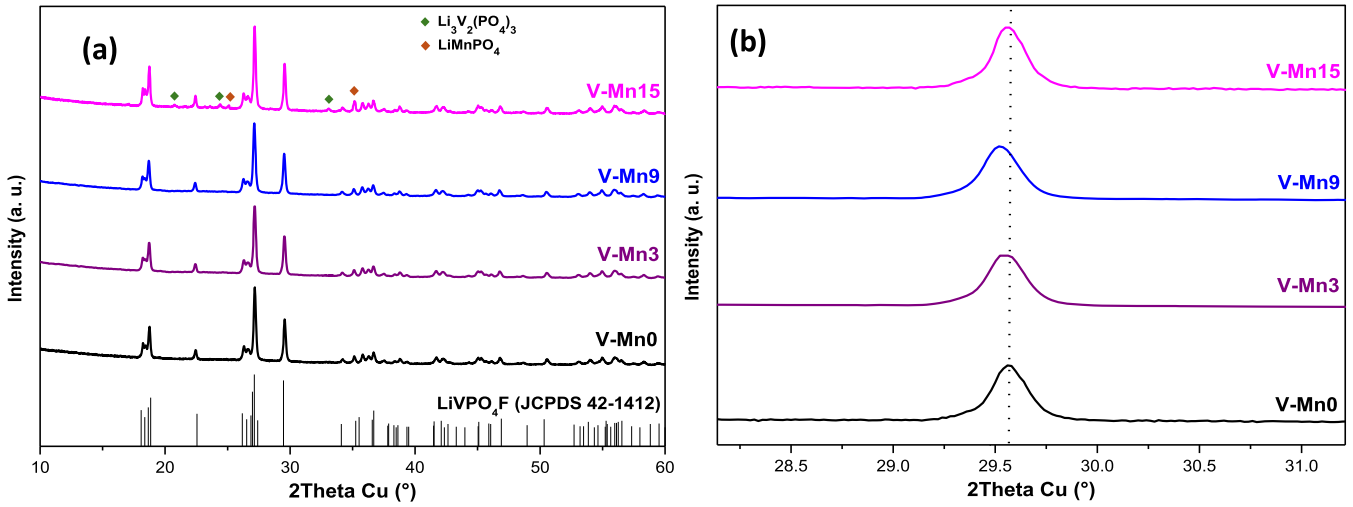

Fig. 3. (a) XRD diffractograms of the synthesized materials. **(b)** Evolution of (1-10) reflection peak with Mn ratio for the synthesized materials.

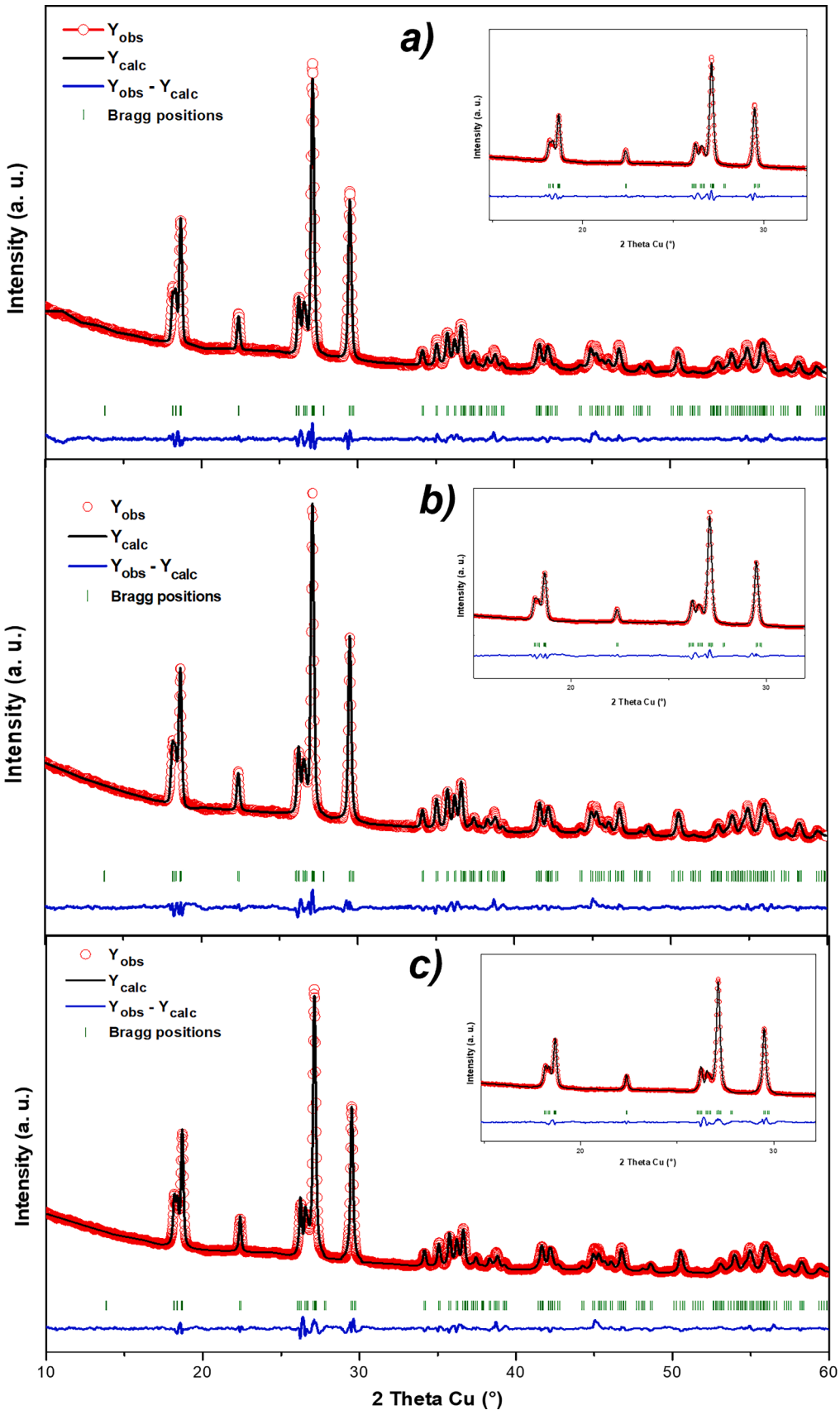

Fig. 4. Rietveld refinement of **(a)** V-Mn0, **(b)** V-Mn3, and **(c)** V-Mn9.

Table 1
The calculated lattice parameters of studied fluorophosphate materials.

Lattice constant	V-Mn0	V-Mn3	V-Mn9	V-Mn15
a	5.241(1) Å	5.271(3) Å	5.342(1) Å	5.251(1) Å
b	7.412(3) Å	7.446(1) Å	7.489(3) Å	7.419(3) Å
c	5.128(1) Å	5.145(2) Å	5.178(4) Å	5.131(2) Å
α	112.97(2) °	113.01(2) °	113.05(4) °	112.99(4) °
β	81.69(2) °	81.73(3) °	81.79(1) °	81.74(2) °
γ	113.15(1) °	113.19(3) °	113.25(2) °	113.14(1) °
V	172.67(1) Å^3	174.82(2) Å^3	179.93(3) Å^3	176.15(3) Å^3

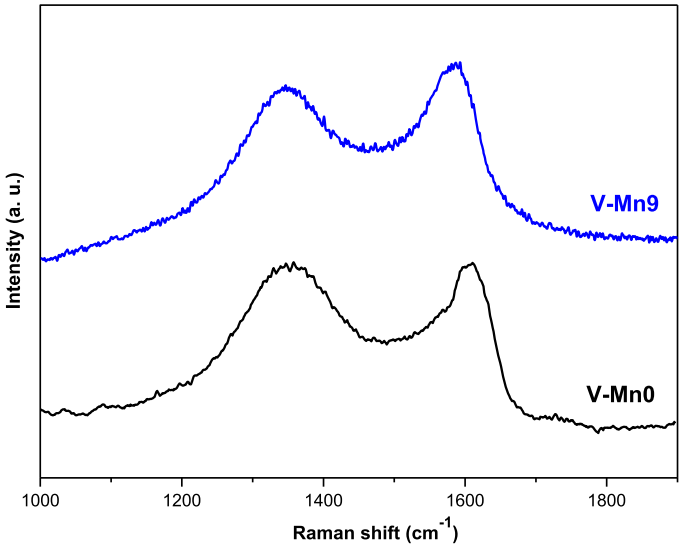

Fig. 5. Raman spectra of the samples V-Mn0 and V-Mn9 between 1000 cm-1 and 1900 cm-1.

phase located at 29.56° for the undoped sample, undergoes a subtle but noticeable shift towards lower 2θ angles as the Mn content increases up to $y = 0.09$. This shift is consistent with lattice expansion due to the larger ionic radius of Mn^{2+} compared to V^{3+}, indicating successful incorporation of Mn into the $LiVPO_4F$ structure. The (1–10) peak is particularly significant because it directly reflects changes in the crystal lattice parameters, providing clear evidence of Mn doping-induced structural modifications. However, at $y = 0.15$, the peak position shifts back towards higher 2θ values, almost aligning with the undoped sample.

The crystal structure refinement of the experimental diffractograms of $LiV_{1-2y/3}Mn_yPO_4F/C$ was performed using the Rietveld method (Fig. 4). As listed in Table 1, the refined lattice parameters of the undoped $LiVPO_4F/C$ are in good agreement with those reported in the literature [35,36]. With Mn doping, the unit cell volume initially expands as Mn is introduced. However, at a higher Mn ratio ($y = 0.15$), a slight decrease in unit cell volume is observed. This anomalous behavior is likely due to the presence of impurity phases in the sample, which disrupt the crystal structure and result in an overall reduction in cell volume.

Fig. 5 shows the Raman spectra of V-Mn0 and V-Mn9 samples, between 1000 and 1900 cm^{-1}. Two main bands are observed: d-band centered around 1350 cm^{-1} and G-band at around 1600 cm^{-1} [37]. This result indicates the carbon formation during the high temperature treatment, primarily from the citric acid used in the synthesis process. Both bands have almost the same intensity ($I_D/I_G \approx 1$ with respect to peak height), suggesting an approximately equal presence of both graphitic and disordered carbon components in the material after the thermal treatment. The dominance of these carbon-related bands in the Raman spectrum (1000–1900 cm^{-1}) confirms that the high-temperature calcination process effectively converted the citric acid into a conductive carbon network within the materials. The in-situ formed carbon, generated through the strategic use of citric acid in the synthesis, likely plays a key role in improving the material's electronic conductivity and overall electrochemical performance.

The SEM image (Fig. 6**. (a)**) reveals well-defined nanoscale particles synthesized via the sol-gel method. The particles exhibit relatively uniform spherical morphology with diameters ranging from approximately 40 to 100 nm (as indicated by the measurements D1-D6), demonstrating good control over particle size and morphology during synthesis.

EDX elemental mapping of the undoped sample (V-Mn0) in Fig. 6. (b) reveals a uniform distribution of V, P, O, and F, confirming the formation of LiVPO4F. More significantly, the EDX mapping of the Mn-doped sample (V-Mn9) in Fig. 6**. (c)** demonstrates the homogeneous distribution of Mn throughout the material, as evidenced by the uniform yellow contrast in the Mn mapping. The homogeneous distribution of Mn indicates the successful incorporation of the dopant into the $LiVPO_4F$ crystal lattice, aligning with the XRD results mentioned earlier, and suggesting minimal segregation or secondary phase formation.

3.2. *Electrochemistry*

Fig. 7 displays slow-rate cyclic voltammograms of samples V-Mn0, V-Mn9, and V-Mn15, measured at a scan rate of 0.1 mV/s, within the voltage range of 3 to 4.6 V versus Li/Li$^+$. For the undoped V-Mn0, the cyclic voltammogram shows oxidation peaks at 4.26 V and 4.32 V, corresponding to the formation of the intermediate phase $Li_{0.65}VPO_4F$ and the fully delithiated phase VPO_4F, respectively. During discharge, a single reduction peak at 4.16 V was observed, corresponding to the re-intercalation of Li$^+$ into VPO_4F to form $LiVPO_4F$. This asymmetric redox behavior suggests variations in lithiation and delithiation pathways or crystallographic differences in Li sites within the structure [35, 36]. V-Mn9 exhibits a similar profile, indicating the preservation of the fundamental redox processes associated with the undoped phase. However, V-Mn9 shows a slight polarization decrease (as shown also in Fig. 8), manifested as a reduction in the potential difference between the anodic and cathodic peaks. suggesting enhanced charge transfer kinetics and improved reversibility of the lithium insertion/extraction process in V-Mn9 material. For the sample V-Mn15, the voltammogram reveals three additional weak redox couples located at 3.60 V / 3.57 V, 3.69 V / 3.65 V, and 4.10 V / 4.02 V (vs. Li/Li+), corresponding to the (de) lithiation processes in the impurity phase $Li_3V_2(PO_4)_3$ [38]. Interestingly, no redox peaks attributable to Mn in $LiMnPO_4$ phase were observed, likely due to the electrochemical inactivity of Mn ions within the investigated potential window. Alternatively, at relatively low ratios, Mn related peaks may be concealed by the broad and intense redox peaks associated with vanadium. This hypothesis is supported by the close proximity of Mn^{2+}/Mn^{3+} and V^{3+}/V^{4+} redox potentials in fluorophosphate-based structures [39,40].

Figs. 8 and 9 display the galvanostatic charge and discharge voltage profiles and the corresponding capacities of the studied materials at a rate of C/5 and 1C, respectively, over 100 cycles. The undoped V-Mn0 exhibits two charge plateaus and one discharge plateau, consistent with the CV measurements. It delivers a discharge capacity of 147 mAh/g, with <2 % capacity fade after 100 cycles and nearly 98 % coulombic efficiency. The Mn-doped materials display similar cycling profiles, except for V-Mn15, which exhibits additional short plateaus attributable to the $Li_3V_2(PO_4)_3$ impurity phase. The V-Mn9 sample delivers the highest discharge capacity of 150 mAh/g, which is almost equivalent to the total theoretical capacity (153 mAh/g) of the material with 98 % capacity retention after 100 cycles. Notably, all samples demonstrate near-ideal coulombic efficiency and very low-capacity fade after 100 cycles. At 1C rate during discharge, V-Mn9 delivers an improved capacity of 146.5 mAh/g compared to 140.3 mAh/g for V-Mn3 and 142.38 mAh/g for the undoped V-Mn0. Interestingly, all cathode materials

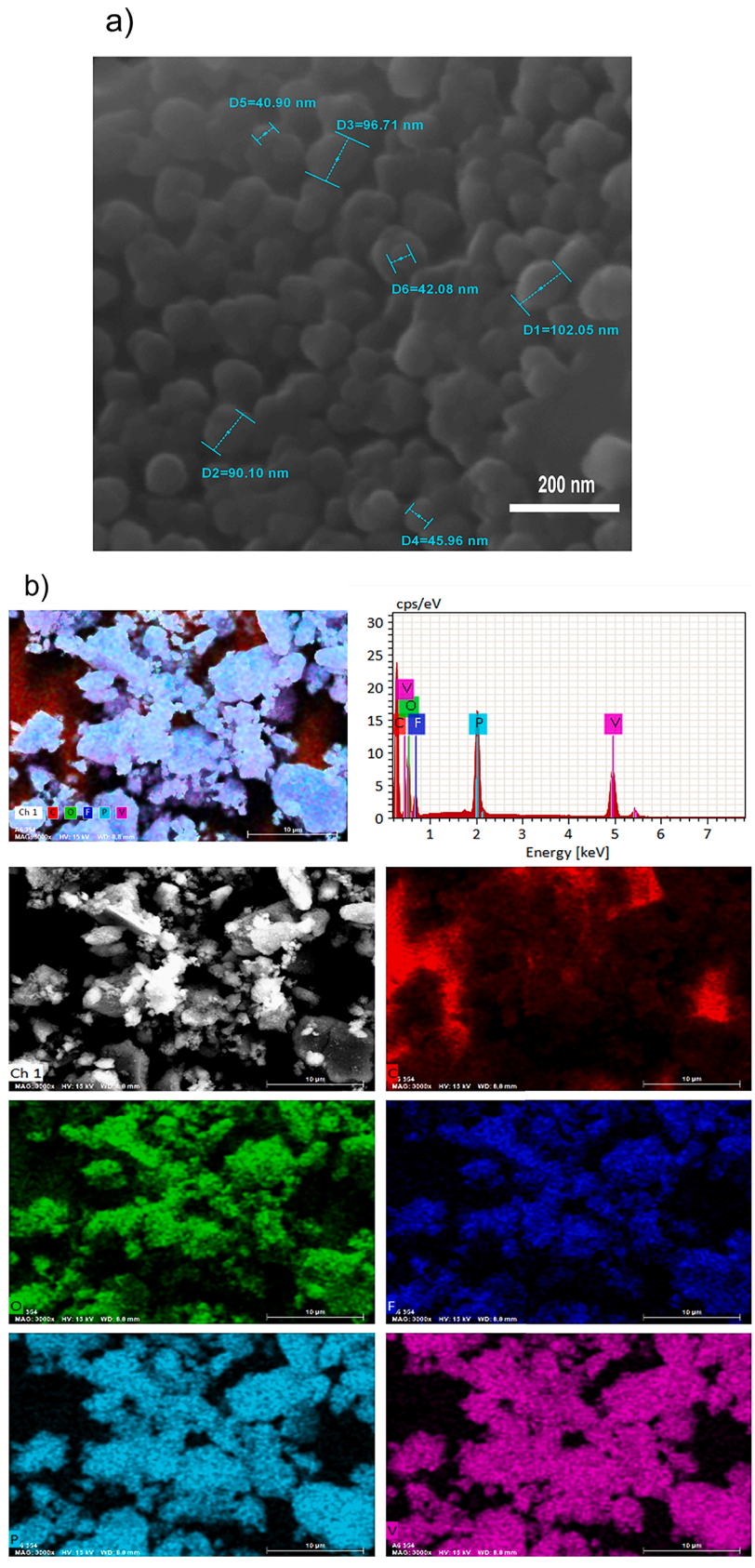

Fig. 6. **(a)**SEM images of V-Mn0, **(b)** element distribution of V-Mn0 and, **(c)** element distribution of V-Mn9.

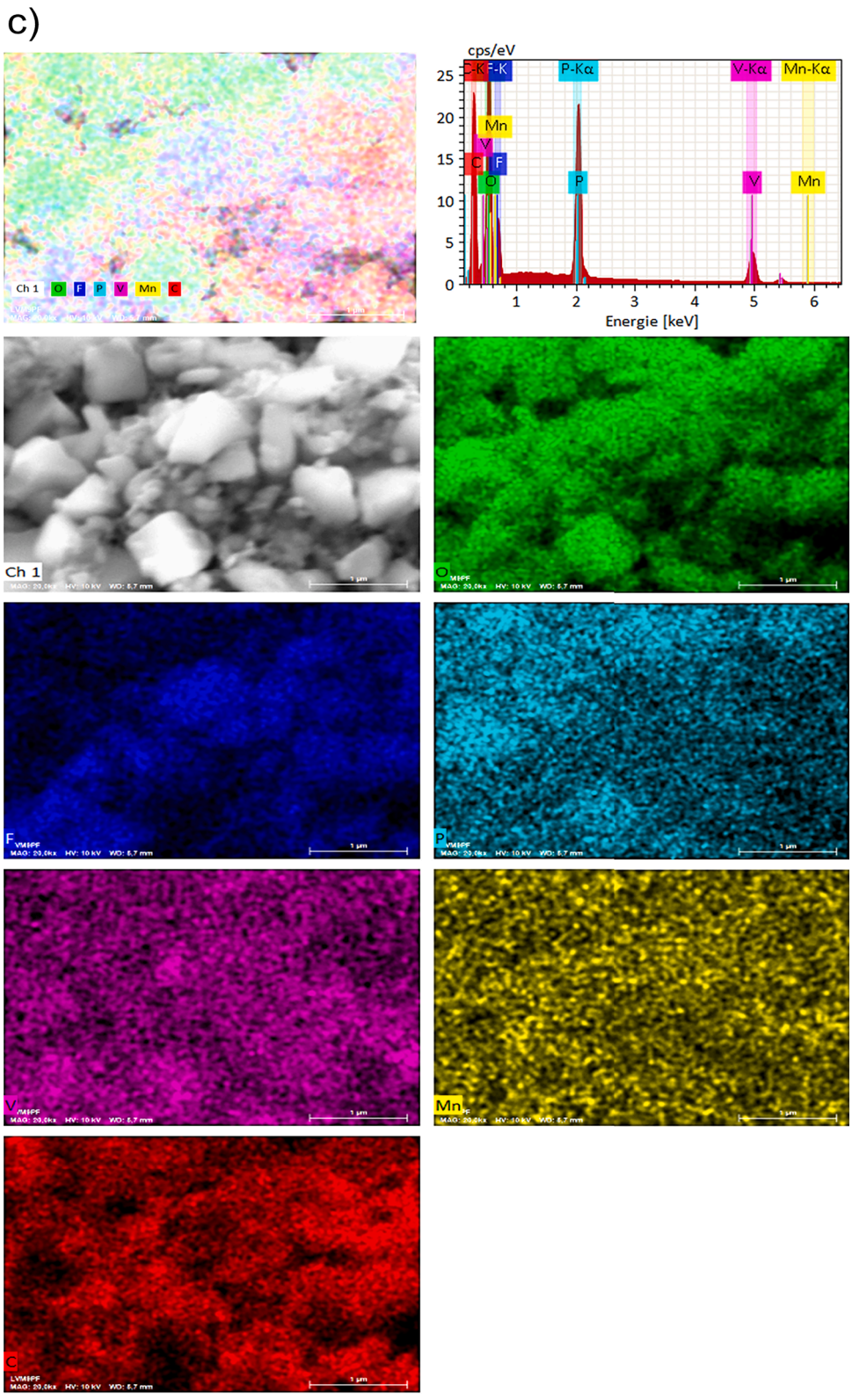

Fig. 6. (*continued*).

preserve an excellent reversibility throughout the electrochemical cycling. The superior performance of V-Mn9 suggests that Mn doping enhances the material's electrochemical properties, likely through structural modifications that create additional pathways for lithium-ion diffusion, thereby improving intrinsic ionic conductivity [41]. Additionally, the band gap of the material can be narrowed by Mn doping, potentially enhancing its electronic conductivity. Furthermore, the nanoscale particles, with their high surface area, can enhance the electrode-electrolyte contact and facilitate rapid charge transfer. The shortened Li^+ diffusion paths within the particles may reduce internal resistance and strain during cycling, contributing to the observed cycling stability [42].

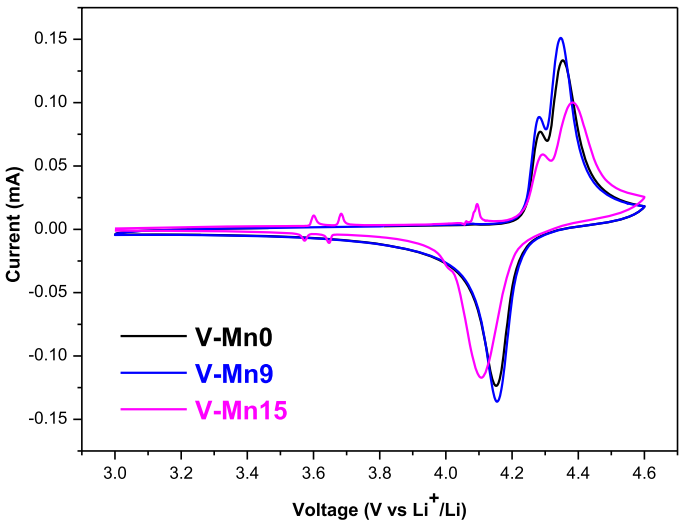

Fig. 7. cyclic voltammograms of the studied fluorophosphate materials.

Fig. 10 displays the electrochemical performance of the studied materials at a rate of C/5 and 50 °C. When cycled at 50 °C, all compositions maintained their characteristic charge-discharge profiles without modification of the voltage plateaus, indicating preserved redox mechanisms and structural stability at higher temperatures. .V-Mn9 sample maintained its superior performance, delivering an initial discharge capacity of 149 mAh/g with minimal capacity fade (≈0.7 %) after 50 cycles. Similarly, both the undoped and V-Mn3 samples demonstrated good stability at elevated temperatures, retaining approximately 99.4 % of their initial capacities after 50 cycles.

Fig. 11. **(a)** displays the rate capability test results for $LiV_{1-2y/3}Mn_yPO_4F/C$ cathode materials, evaluated at C/5, 1C, 2C, 3C, and 5C, and then returning back to C/5. The undoped material presents an initial discharge capacity of 147 mAh/g and exhibits excellent capacity retention of approximately 97 % upon cycling back to C/5 after high-rate testing. The V-Mn3 sample displays an intriguing performance, showing lower discharge capacities at lower C-rates but superior capacity retention at 5C. The V-Mn9 sample exhibited superior performance across all tested C-rates, maintaining high capacities from C/5 to 5C and showing almost identical capacity when cycled back to C/5. Additionally, as illustrated in Fig. 10. **(b)**, V-Mn9 exhibits the lowest voltage polarization at 5C among all samples. The overall stable performance of these materials can be linked to the materials' stable crystal structure and optimized morphology. Moreover, Mn incorporation further enhances electrochemical performance, likely by improving intrinsic ionic and electronic conductivity [41,42].

In order to evaluate the impact of Mn addition on the kinetics of the studied electrode materials, the lithium ion diffusion was calculated.

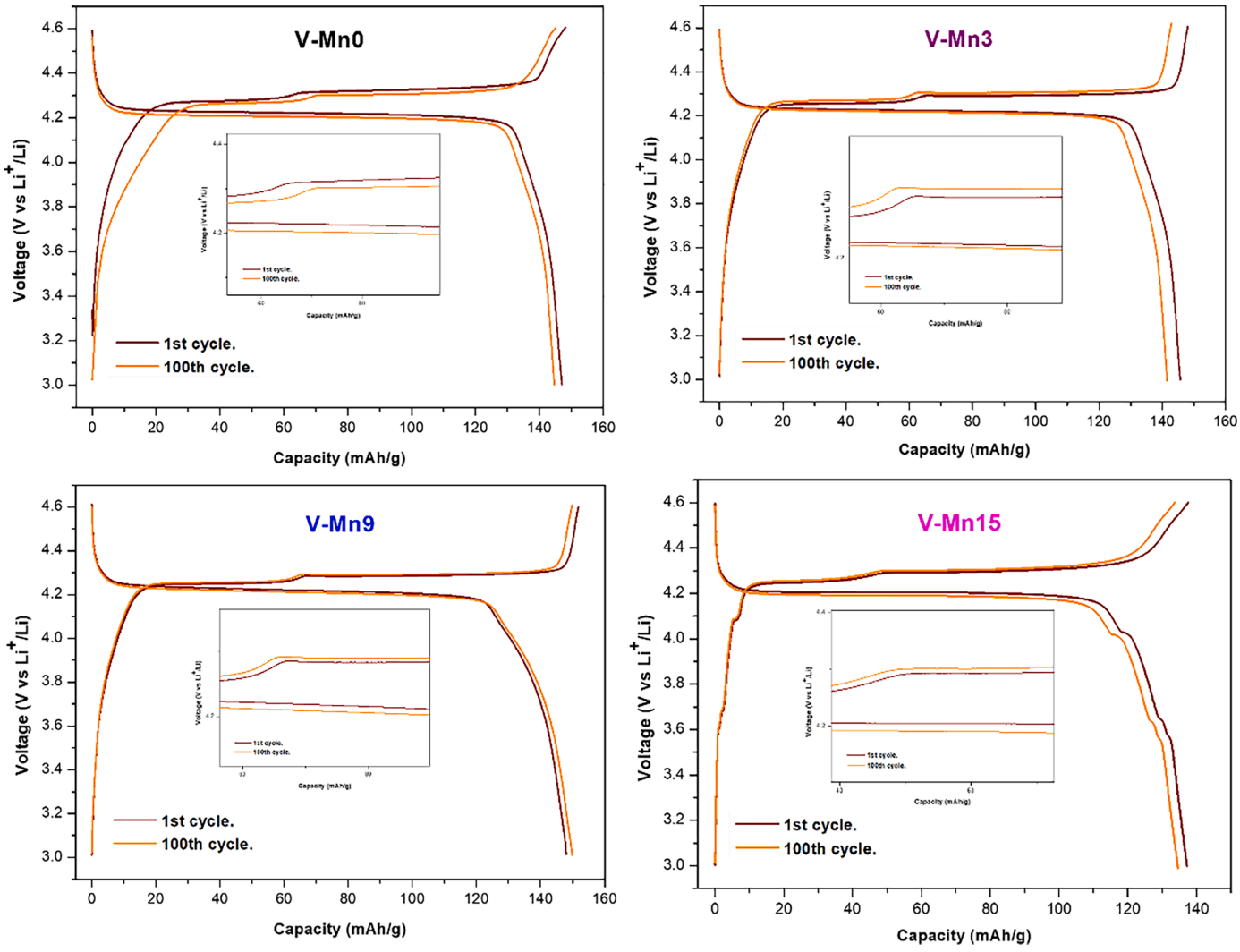

Fig. 8. Galvanostatic cycling profiles of the studied materials at a rate of C/5.

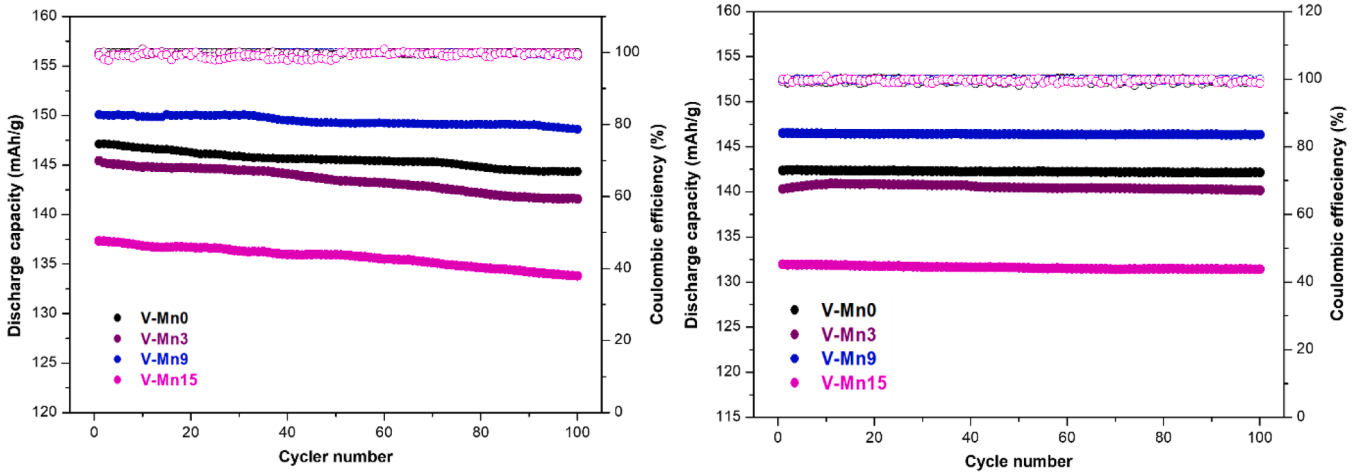

Fig. 9. Specific discharge capacities of the studied materials over 100 cycles at **(a):** C/5 rate; **(b):** 1C rate.

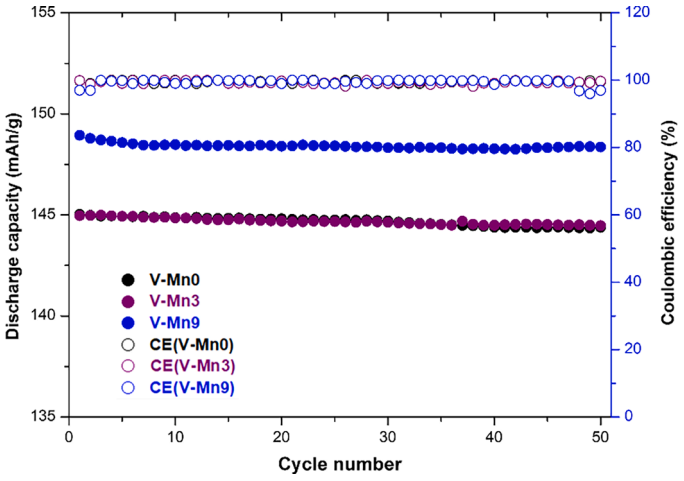

Fig. 10. Electrochemical cycling of the studied materials at C/5 rate and 50°C.

Fig. 12 shows the multi-rate cyclic voltammetry (CV) responses of V-Mn0 and V-Mn9 electrodes at various scan rates. The peak currents (Ip) increase with increasing scan rate (ν), exhibiting a linear relationship between i_p and $\nu^{1/2}$. This linear behavior suggests that the redox process is primarily controlled by lithium diffusion. The lithium diffusion coefficient (D_{Li+}) was calculated using the **Randles-Sevcik equation** based on the measured current values.

$$ip = 0.4463\left(\frac{F^3}{RT}\right)^{\frac{1}{2}} n^{3/2} A D^{1/2} C_0^* \nu^{1/2}$$

$$\frac{ip}{\nu^{1/2}} = b \cdot D^{1/2} ; b = 0.4463\left(\frac{F^3}{RT}\right)^{\frac{1}{2}} n^{3/2} C_0^*$$

where i_p is the peak current value, n is the number of exchanged electrons, F is the Faraday constant, A is the electrode geometric area (1.13 cm^2), C_0* is the Li^+ concentration within the material lattice (mol cm^{-3}), ν is the scan rate (V s^{-1}), R is the gas constant (J K^{-1} mol^{-1}), and T is the temperature (K) [43].

Based on the calculated diffusion coefficients presented in Table 2, a clear trend emerges between the undoped V-Mn0 and V-Mn9. For Li^+ ion extraction, V-Mn9 exhibits a slightly higher diffusion coefficient of 2.87(1) × 10^{-9} cm^2 s^{-1} compared to 2.67(2) × 10^{-9} cm^2 s^{-1} for V-Mn0.

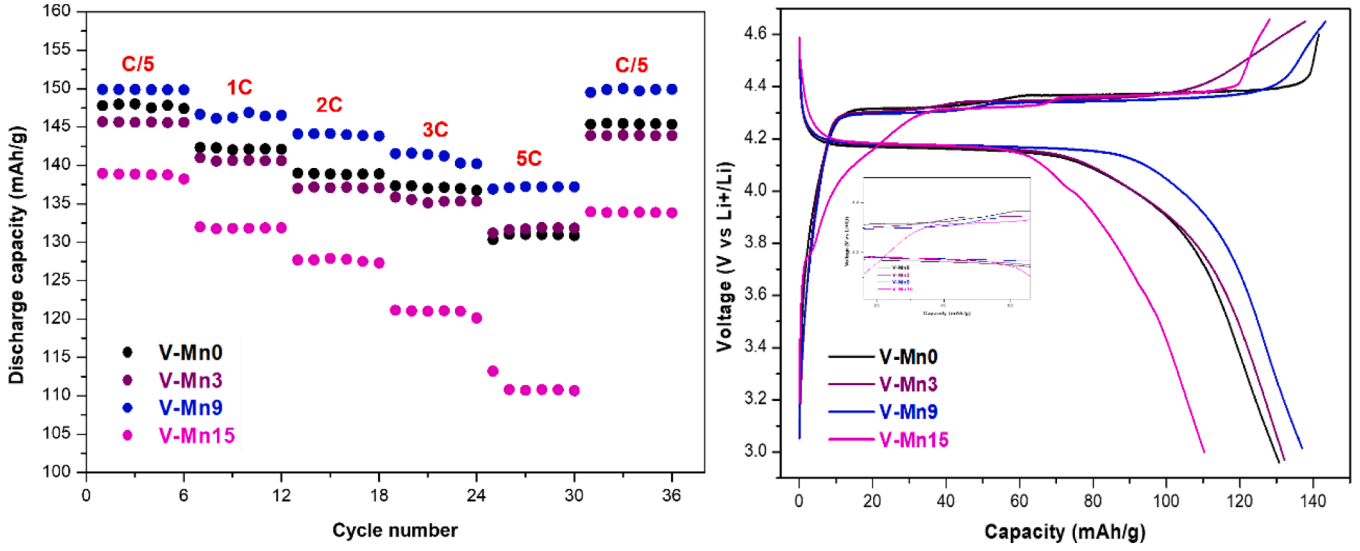

Fig. 11. **(a)** Rate capability test of the studied materials. **(b)** Galvanostatic cycling profiles of the studied materials at a rate of 5C.

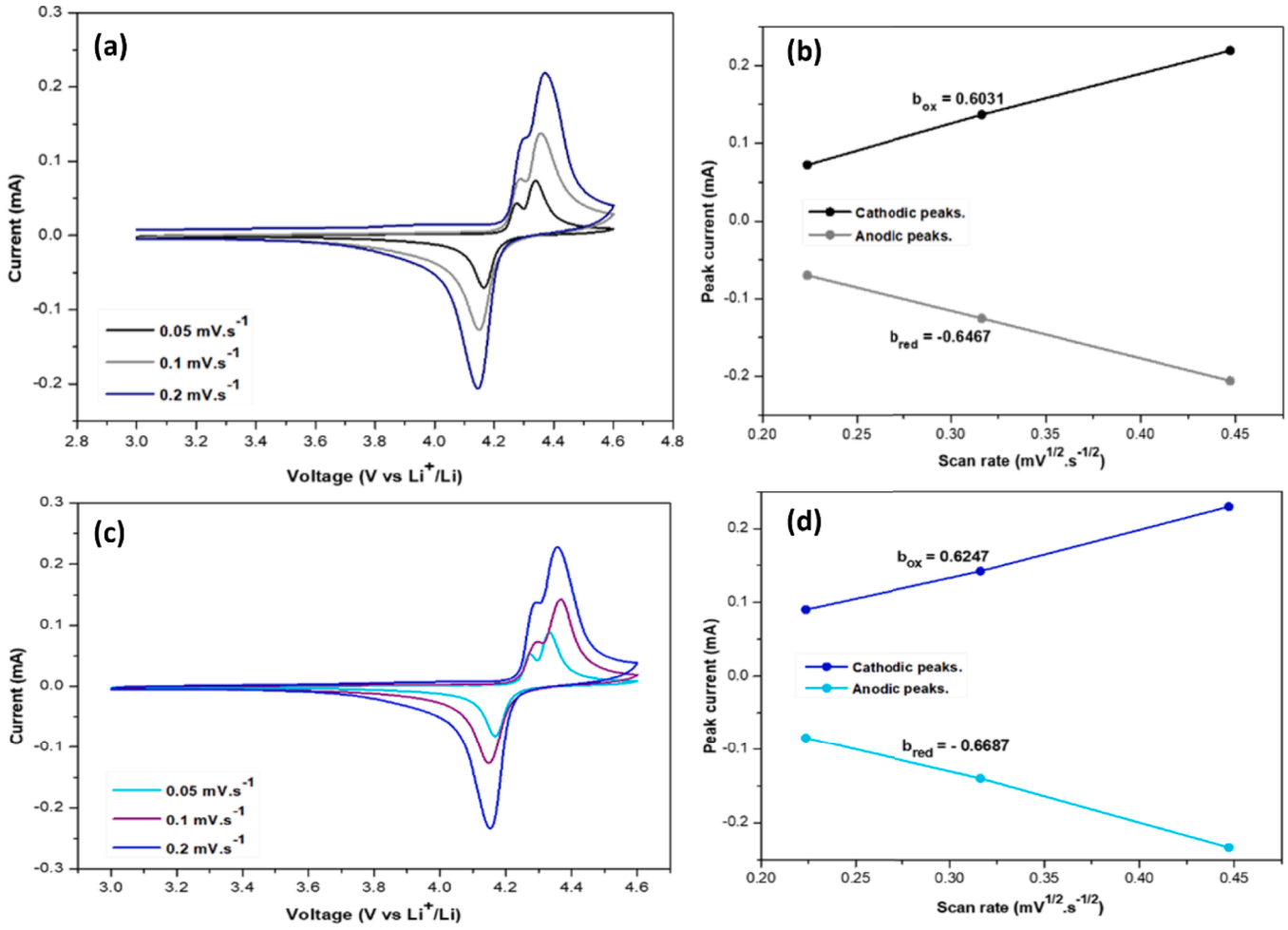

Fig. 12. **(a)** CV responses at different scan rates for V-Mn0. **(b)** plot of cathodic and anodic peak currents versus $v^{1/2}$ for V-Mn0. **(c)** CV responses at different scan rates for V-Mn9. **(d)** plot of cathodic and anodic peak currents versus $v^{1/2}$ for V-Mn9.

Table 2
The calculated diffusion coefficients for V-Mn0 and V-Mn9.

	D^{+}_{Li} ($cm^2\ s^{-1}$) (V-Mn0)	D^{+}_{Li} ($cm^2\ s^{-1}$) (V-Mn9)
Li^+ ions extraction	$2.67(2) \times 10^{-9}$	$2.87(1) \times 10^{-9}$
Li^+ ions insertion	$3.07(3) \times 10^{-9}$	$3.29(3) \times 10^{-9}$

Similarly, during Li^+ ion insertion, V-Mn9 shows an enhanced diffusion coefficient of $3.29(3) \times 10^{-9}$ $cm^2\ s^{-1}$ versus $3.07(3) \times 10^{-9}$ $cm^2\ s^{-1}$ for V-Mn0.

This improved diffusion kinetics provide critical insight into the rate capability results shown in Fig. 11. (a). The enhanced Li+ transport in V-Mn9 manifests as superior electrochemical performance, particularly at high C-rates where diffusion limitations typically become pronounced. When cycling at 5C, the faster Li+ movement within the crystal structure of V-Mn9 enables more efficient charge transfer at the electrode-electrolyte interface, reducing concentration polarization and maintaining higher accessible capacity. This phenomenon is further supported by the reduced voltage hysteresis observed in Fig. 11. (b) for the V-Mn9 sample.

The higher diffusion coefficients observed in the Mn-doped sample indicate that Mn incorporation enhances lithium-ion transport within the crystal structure, probably due to the expansion of the crystal lattice. Notably, both materials demonstrate superior diffusion kinetics compared to previously reported values in the literature for phosphate and fluorophosphate materials (typically ranging from 10^{-12} to 10^{-10} $cm^2\ s^{-1}$), indicating excellent Li^+ mobility in these materials [44–47].

4. Conclusions

$LiV_{1-2y/3}Mn_yPO_4F/C$ ($y = 0$, 0.03, 0.09, 0.15) cathode materials were successfully synthesized using a one-step sol-gel method. XRD analysis confirmed the formation of phase-pure materials with a triclinic structure up to $y = 0.09$. However, higher Mn content ($y = 0.15$) resulted in the formation of secondary phases. The optimized composition ($y = 0.09$) delivered an improved discharge capacity of 150 mAh/g at C/5, approaching the theoretical capacity of 153 mAh/g, with 98 % capacity retention after 100 cycles. At elevated temperature (50 °C), the material maintained excellent stability, with minimal capacity fade (< 1 %) after 50 cycles. Rate capability tests demonstrated superior performance of the Mn-doped samples, particularly at higher C-rates, with the $y = 0.09$ sample maintaining high capacities from C/5 to 5C. The enhanced rate performance can be attributed to improved Li^+ ion diffusion kinetics in the Mn-doped material, as demonstrated by higher diffusion coefficients compared to the undoped sample. These results establish Mn-doping as an effective strategy for enhancing the electrochemical performance of $LiVPO_4F$-based cathode materials for high-voltage lithium-ion batteries.

CRediT authorship contribution statement

Ismail Assengar: Writing – review & editing, Writing – original draft, Investigation, Formal analysis, Data curation. **Sylvio Indris:** Writing – review & editing, Validation, Supervision, Formal analysis.

Arseniy Bokov: Writing – original draft, Validation, Data curation. **Liuda Mereacre:** Writing – review & editing, Formal analysis. **Mohammed Mansori:** Writing – review & editing, Methodology, Funding acquisition. **Ismael Saadoune:** Writing – review & editing, Validation, Methodology, Funding acquisition, Conceptualization.

Declaration of competing interest

The authors declare the following financial interests/personal relationships which may be considered as potential competing interests: Ismael SAADOUNE reports financial support was provided by OCP Foundation. If there are other authors, they declare that they have no known competing financial interests or personal relationships that could have appeared to influence the work reported in this paper.

Acknowledgments

The authors acknowledge with gratitude the financial support provided by the Moroccan Ministry of Higher Education, Scientific Research, and Innovation, Mohammed VI Polytechnic University, the OCP Foundation through the APRD Research Program (2022–2025).

Data availability

Data will be made available on request.

References

[1] D.A. Notter, et al., Contribution of Li-ion batteries to the Environmental Impact of Electric Vehicles, ACS Publications, 2010, https://doi.org/10.1021/es903729a.
[2] C. Daniel, et al., Cathode materials review, in: AIP Conference Proceedings, American Institute of Physics, 2014, https://doi.org/10.1063/1.4878478.
[3] Dixit, A., Cathode materials for lithium ion batteries (LIBs): a review on materials related aspects towards high energy density LIBs. arXiv preprint, 2020. https://doi.org/10.48550/arXiv.2008.10896.
[4] P. Rozier, J.M. Tarascon, Li-rich layered oxide cathodes for next-generation Li-ion batteries: chances and challenges, J. Electrochem. Soc. 162 (14) (2015) A2490, https://doi.org/10.1149/2.0111514jes.
[5] T.-F. Yi, J. Mei, Y.-R. Zhu, Key strategies for enhancing the cycling stability and rate capacity of LiNi0. 5Mn1. 5O4 as high-voltage cathode materials for high power lithium-ion batteries, J. Power Sources 316 (2016) 85–105, https://doi.org/10.1016/j.jpowsour.2016.03.070.
[6] P. Stüble, et al., On the composition of LiNi0. 5Mn1. 5O4 cathode active materials, Adv. Energy Mater. 13 (10) (2023) 2203778, https://doi.org/10.1002/aenm.202203778.
[7] J.H. Kim, N.P. Pieczonka, L. Yang, Challenges and approaches for high-voltage spinel lithium-ion batteries, ChemPhysChem. 15 (10) (2014) 1940–1954, https://doi.org/10.1002/cphc.201400052.
[8] S.S. Jayasree, et al., Recent progress on the low and high temperature performance of nanoscale engineered Li-ion battery cathode materials, Nanotechnology. 33 (35) (2022) 352001, https://doi.org/10.1088/1361-6528/ac67ac.
[9] Z. Gong, Y. Yang, Recent advances in the research of polyanion-type cathode materials for Li-ion batteries, Energy Environ. Sci. 4 (9) (2011) 3223–3242, https://doi.org/10.1039/c0ee00713g.
[10] S. El Moutchou, et al., Thermal stability of Lithium-ion batteries: case study of NMC811 and LFP cathode materials, in: Materials Today: Proceedings 51, 2022, pp. A1–A7, https://doi.org/10.1016/j.matpr.2022.02.324.
[11] Yiqing, H., et al., Thermal stability and reactivity of cathode materials for Li-ion batteries. 2016 DOI: https://doi.org/10.1021/acsami.5b12081.
[12] K. Akhmetova, et al., Advances in multi-element doping of LiFePO4 cathode material for capacity enhancement in Li-ion batteries, J. Power Sources 624 (2024) 235531, https://doi.org/10.1016/j.jpowsour.2024.235531.
[13] L. Sharma, et al., Fluorophosphates: next generation cathode materials for rechargeable batteries, Adv. Energy Mater. 10 (43) (2020) 2001449, https://doi.org/10.1002/aenm.202001449.
[14] M. Hadouchi, et al., Fluorophosphates and fluorosulfates cathode materials: progress towards high energy density sodium-ion battery, Nano Res. 17 (3) (2024) 1427–1440, https://doi.org/10.1007/s12274-023-6005-3.
[15] W. Zhang, et al., Construction of superior performance LiVPO4F/C cathode assisting by a regulating additive NH4F and the "Combination-Protection-Release" mechanism for lithium ion batteries, J. Power Sources 523 (2022) 231024, https://doi.org/10.1016/j.jpowsour.2022.231024.
[16] J.-M. Ateba Mba, et al., Synthesis and crystallographic study of homeotypic LiVPO4F and LiVPO4O, Chem. Mater. 24 (6) (2012) 1223–1234, https://doi.org/10.1021/cm3003996.
[17] J. Barker, et al., Structural and electrochemical properties of lithium vanadium fluorophosphate, LiVPO4F, J. Power Sources 146 (1–2) (2005) 516–520, https://doi.org/10.1016/j.jpowsour.2005.03.126.
[18] Z.Z. LI YZ, X. GAO, J. YAN, A novel sol-gel method to synthesize nanocrystalline LiVPO4F and its electrochemical Li intercalation performances, J. Power Sources 160 (1) (2006) 633–637, https://doi.org/10.1016/j.jpowsour.2006.01.067.
[19] M. Kim, S. Lee, B. Kang, Fast-rate capable electrode material with higher energy density than LiFePO4: 4.2 V LiVPO4F synthesized by scalable single-step solid-State reaction, Adv. Sci. 3 (3) (2016) 1500366, https://doi.org/10.1002/advs.201500366.
[20] Q. Li, et al., Chemical reaction characteristics, structural transformation and electrochemical performances of new cathode LiVPO 4 F/C synthesized by a novel one-step method for lithium ion batteries, RSC. Adv. 8 (13) (2018) 7044–7054, https://doi.org/10.1039/C8RA00370J.
[21] X. Zhang, et al., Effects of Fe doping on the electrochemical performance of LiV1 x Fe x PO4F/C (x= 0, 0.01, 0.02, 0.04) cathode materials for lithium-ion batteries, J. Chin. Chem. Soc. 69 (5) (2022) 786–793, https://doi.org/10.1002/jccs.202200086.
[22] Z. Peng, et al., Electrochemical performance of Co-doped LiVPO4F/C composite cathode material for lithium ion batteries prepared by modified solid state method, J. Alloys. Compd. 730 (2018) 261–269, https://doi.org/10.1016/j.jallcom.2017.09.333.
[23] S. Zhong, et al., Preparation and electrochemical studies of Y-doped LiVPO 4 F cathode materials for lithium-ion batteries, J. Wuhan Univ. Technol. Mater. Sci. Ed. 24 (2009) 552–556, https://doi.org/10.1007/s11595-009-4552-4.
[24] G. Hu, et al., Multi-level carbon co-modified LiVPO4F cathode material for lithium batteries, J. Alloys. Compd. 788 (2019) 1146–1153, https://doi.org/10.1016/j.jallcom.2019.02.323.
[25] B. Yang, L. Yang, Silver-coated LiVPO4F composite with improved electrochemical performance as cathode material for lithium-ion batteries, J. Phys. Chem. Solids 87 (2015) 228–232, https://doi.org/10.1016/j.jpcs.2015.07.013.
[26] X. Yang, et al., Improved Li-storage performance of CNTs-decorated LiVPO4F/C cathode material for electrochemical energy storage, Ceram. Int. 44 (4) (2018) 3825–3829, https://doi.org/10.1016/j.ceramint.2017.11.168.
[27] W.-h. Zhang, et al., High-performance LiVPO4F/C cathode constructed by using polyvinylidene fluoride as carbon source and the influencing mechanism for lithium ion batteries, J. Alloys. Compd. 778 (2019) 345–358, https://doi.org/10.1016/j.jallcom.2018.11.151.
[28] Y.-L. Sui, et al., Synthesis and electrochemical properties of spherically shaped LiVPO 4 F/C cathode material by a spray drying–roasting method, Rare Metals. 40 (2021) 72–77, https://doi.org/10.1007/s12598-019-01340-0.
[29] T. Zeng, et al., Rational design of a LiVPO4F@ C microsphere cathode enabled by a one-step hydrothermal reaction for lithium-ion batteries, ACS. Sustain. Chem. Eng. 12 (9) (2024) 3643–3651, https://doi.org/10.1021/acssuschemeng.3c06926.
[30] J.-S. Park, et al., Effect of Mn in Li3V2–x Mn x (PO4) 3 as high capacity cathodes for lithium batteries, ACS. Appl. Mater. Interfaces. 9 (46) (2017) 40307–40316, https://doi.org/10.1021/acsami.7b13128.
[31] Z. Ting, M.-S. Zhao, D.-D. Wang, Effect of Mn-doping on performance of Li3V2 (PO4) 3/C cathode material for lithium ion batteries, Trans. Nonferrous Metals Soc. China 21 (3) (2011) 523–528, https://doi.org/10.1016/S1003-6326(11)60746-2.
[32] G. Minart, et al., New Mn and V-rich phosphate fluoride obtained by topochemical reaction for Na-ion batteries positive electrode, Chem. Mater. 36 (20) (2024) 10186–10197, https://doi.org/10.1021/acs.chemmater.4c01833.
[33] W. Shen, et al., Improvement On the High-Rate Performance of Mn-doped Na 3 V 2 (PO 4) 3/C As a Cathode Material For Sodium Ion Batteries, 6, RSC advances, 2016, pp. 71581–71588, https://doi.org/10.1039/c6ra16515j.
[34] K. Cui, S. Hu, Y. Li, Nitrogen-doped graphene-decorated LiVPO4F nanocomposite as high-voltage cathode material for rechargeable lithium-ion batteries, J. Power Sources 325 (2016) 465–473, https://doi.org/10.1016/j.jpowsour.2016.06.058.
[35] B.L. Ellis, et al., Structure and electrochemistry of two-electron redox couples in lithium metal fluorophosphates based on the tavorite structure, Chem. Mater. 23 (23) (2011) 5138–5148, https://doi.org/10.1021/cm201773n.
[36] T.C. Lin, et al., Fast-charging cathodes from polymer-templated mesoporous LiVPO4F, ACS. Appl. Mater. Interfaces. 12 (30) (2020) 33775–33784, https://doi.org/10.1021/acsami.0c08709.
[37] H. Aziam, et al., Synthesis, characterization, electrochemistry, and in situ X-ray diffraction investigation of Ni3 (PO4) 2 as a negative electrode material for lithium-ion batteries, ChemElectroChem. 7 (18) (2020) 3866–3873, https://doi.org/10.1002/celc.202001065.
[38] X. Rui, et al., Li3V2 (PO4) 3 cathode materials for lithium-ion batteries: a review, J. Power Sources 258 (2014) 19–38, https://doi.org/10.1016/j.jpowsour.2014.01.126.
[39] J.-W. Lee, et al., Electrochemical lithiation and delithiation of LiMnPO4: effect of cation substitution, Electrochim. Acta 55 (13) (2010) 4162–4169, https://doi.org/10.1016/j.electacta.2010.02.097.
[40] G. Li, H. Azuma, M. Tohda, LiMnPO4 as the cathode for lithium batteries, Electrochem. Solid-State Lett. 5 (6) (2002) A135, https://doi.org/10.1149/1.1475195.
[41] F. Jiang, et al., Atomic scale insight into the fundamental mechanism of Mn doped LiFePO 4, Sustain. Energy Fuels 4 (6) (2020) 2741–2751, https://doi.org/10.1039/d0se00312c.
[42] C. Ahmani Ferdi, M. Belaiche, E. Iffer, Structural, electrochemical, electronic, and magnetic properties of monoclinic Li x V 2 (PO 4) 3 for x= 3, 2, 1 using first-principles calculations, J. Solid State Electrochem. 25 (2021) 301–313, https://doi.org/10.1007/s10008-020-04808-7.

[43] D. Di Lecce, J. Hassoun, Lithium transport properties in LiMn1 αFeαPO4 olivine cathodes, J. Phys. Chem. C 119 (36) (2015) 20855–20863, https://doi.org/10.1021/acs.jpcc.5b06727.
[44] M.T. Nguyen, et al., Effect of conductive carbon additives and negative/positive capacity ratio on graphite/LiFePO4 full-cells performance, Energy Storage 5 (6) (2023) e449.
[45] W. Li, et al., Electrochemical performance investigation of LiFePO4/C0.15-x (x=0.05, 0.1, 0.15 CNTs) electrodes at various calcination temperatures: experimental and intelligent modelling approach, Electrochim. Acta 330 (2020) 135314, https://doi.org/10.1016/j.electacta.2019.135314.
[46] Y.-C. Lin, et al., Synthesis and electrochemical properties of xLiFePO4·(1 x) LiVPO4F composites prepared by aqueous precipitation and carbothermal reduction, J. Power Sources 244 (2013) 63–71.
[47] W. Zhang, et al., Construction and theoretical calculation of an ultra-high-performance LiVPO4F/C cathode by B-doped pyrolytic carbon from poly (vinylidene fluoride), ACS. Appl. Mater. Interfaces. 13 (13) (2021) 15190–15204.